Composite Structures 345 (2024) 118342

Contents lists available at ScienceDirect

Composite Structures

journal homepage: www.elsevier.com/locate/compstruct

Tailoring band gap properties of curved hexagonal lattices with nodal cantilevers

Shuvajit Mukherjee [a,*,1], Marcus Maeder [a], Milan Cajić [b], Felix Kronowetter [a], Sondipon Adhikari [c], Steffen Marburg [a]

[a] Chair of Vibroacoustics of Vehicles and Machines, TUM School of Engineering and Design, Technical University of Munich (TUM), Boltzmannstraße 15, 85748 Garching bei Munich, Germany

[b] Mathematical Institute of the Serbian Academy of Sciences and Arts, Kneza Mihaila 36, Belgrade, Serbia

[c] James Watt School of Engineering, The University of Glasgow, Glasgow G12 8QQ, UK

ARTICLE INFO

Keywords:
Hexagonal lattices
Metamaterials
Curved beams
Wave propagation
Band gaps
Bloch's theorem

ABSTRACT

Metamaterials find applications across diverse domains such as electromagnetics, elasticity, and acoustics by creating band gaps. Lattice-based metamaterials also exhibit band gaps, which have a great potential to influence engineering design in vibration and noise reduction problems. The geometry of the repetitive unit cell in the lattice plays a crucial role in diversifying the location and number of stop bands across the frequency range. One of the key hurdles is devising unit cell architectures that can effectively suppress vibrations across diverse frequency ranges. This work proposes an innovative two-dimensional hexagonal lattice with tailored band gap characteristics through curved beam members and auxiliary cantilever beams at the nodes. We have thoroughly explored the impact of various design parameters on dispersion characteristics, wave directionality through iso-frequency contours of dispersion surfaces, and the transmission loss considering finite lattice. The investigation demonstrates an improvement in band gap characteristics, indicating the generation of more band gaps across the entire frequency range and the widening of the same. This study has the potential to serve as a future benchmark in the development of lattice-based elastic/acoustic metamaterials, particularly for addressing vibration reduction challenges at user-defined frequencies.

1. Introduction

Metamaterials have extensive engineering applications due to their distinct mechanical attributes, which are not naturally available [1,2]. The applications of these materials span diverse fields such as structural, aerospace, automobile, civil industries, crystallography, and material sciences [3–5]. Two-dimensionally architectured lattices are also a kind of metamaterial that is formed by tessellating a periodic unit cell. The unit cell's geometry dictates the lattices' material properties [6]. Researchers have exploited different unit cell geometry to develop unique properties such as negative Poisson's ratio, vibration attenuation, shock resistance, noise mitigation, and energy absorption [7–11]. The advent of additive manufacturing has accelerated research on these complex materials, opening the door to designing and manufacturing innovative materials based on specific requirements [12]. In recent years, researchers have actively explored the capabilities of lattice-based metamaterials for addressing vibration attenuation and directional wave propagation challenges [13–15]. Numerous studies have proposed various lattice designs and investigated their properties in terms of wave propagation and dispersion. Triangular and square patterns in one-dimensional [16], and two-dimensional lattices [17], along with hexagonal or re-entrant structures [18] and chiral lattices [19], have been common designs. The unit cell's topologies influence the band structure, directional wave propagation, and wave speed. Besides geometry, external fields such as thermal and magnetic forces and externally applied loads causing structural deformation can also regulate the dispersion pattern. The literature reports instability-driven manipulation of wave propagation behavior [20,21]. Modifying the unit cell's architecture can result in diverse wave propagation behaviors, allowing for the tuning of wave filters. This outcome has influenced researchers in acoustics and structural engineering.

Different research groups have conducted detailed investigations into the propagation of plane waves and directional behavior within hexagonal and re-entrant beam-based lattices [18,19,22]. Apart from the classic geometry for the lattices, researchers have explored new

* Corresponding author.
E-mail addresses: shuvajit@iitj.ac.in, shuvajit.mukherjee@tum.de (S. Mukherjee).
[1] Present address: Department of Civil and Infrastructure Engineering, Indian Institute of Technology Jodhpur, Jodhpur, Rajasthan 342030, India.

https://doi.org/10.1016/j.compstruct.2024.118342
Received 20 December 2023; Received in revised form 21 June 2024; Accepted 2 July 2024
Available online 6 July 2024
0263-8223/© 2024 The Authors. Published by Elsevier Ltd. This is an open access article under the CC BY-NC-ND license (http://creativecommons.org/licenses/by-nc-nd/4.0/).

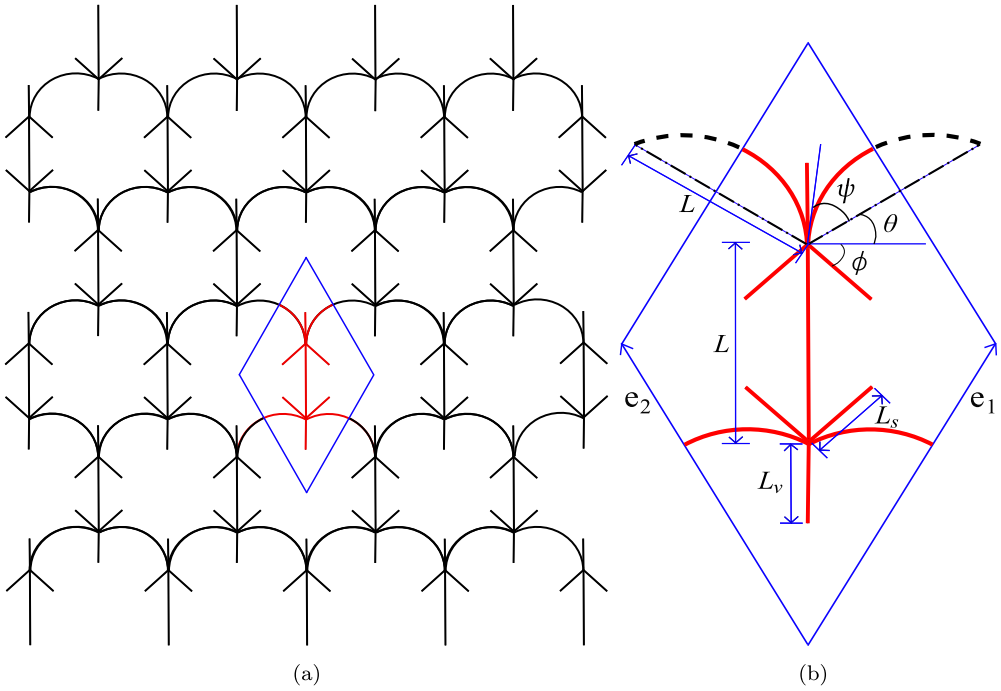

Fig. 1. (a) Hybrid hexagonal lattice and its corresponding unit cell and (b) geometric details of the unit cell: the direct lattice vectors ($\mathbf{e}_1$ and $\mathbf{e}_2$), cell angle θ, curvature angle ψ. inclination angle of the added beam members ϕ, length of the main constituent beam L, and length of the extra added beams (vertical beam L_v, slant beam L_s).

topologies to obtain desired band gap properties [17,23–25]. Mukherjee et al. [26] have proposed a combination of conventional and auxetic cores to widen the band gaps. Furthermore, scholars are interested in developing lattice-based metamaterials that can provide low-frequency vibration reduction [27]. To achieve that both local resonance and Bragg-type gaps or their combination are explored over the period [28–30]. Existing literature demonstrates the manipulation of band gaps by altering the lattice's unit cell through changes in the geometry of constituent beam-like members [31]. The researchers have explored both forward and topology optimization methods to achieve this objective [32–36]. Additionally, fractal-inspired [37,38] and bio-inspired [39] lattice structures are also investigated to understand wave propagation behavior in sub-wavelength frequency ranges. These studies delved into the impact of various geometric parameters on band structures, phase and group velocities, and directional properties, employing Bloch's theory. Researchers consider the irreducible Brillouin zone, obtained by constructing the reciprocal lattice and considering the symmetry of the unit cell of the lattice to obtain the dispersion behavior. Choosing an irreducible Brillouin zone (IBZ) reduces the computational cost for the periodic analysis.

Most works are based on the lattice with straight constituent structural members for the unit cell. Although undulated constituent elements are explored to control the waves in the low and high-frequency regions [40], several types of research can be found, which consist of unit cells with zig-zag elements [41,42] and curved structural elements to manipulate the static, dispersion behavior and directional wave propagation for the lattice [43–45]. There are works on wave propagation for triangular chiral lattices with zig-zag beams [46], hybrid infrastructures with mass inclusion [47], structures with variable cross sections [48], and reentrant-chiral lattices with and without mass inclusion to enhance the wave propagation characteristics [49–51]. Recently, Mukherjee et al. [52] have proposed a modified hexagonal and re-entrant hexagonal lattice considering the combination of straight and curved beams for the unit cell. It influenced the band gap characteristics, obtaining more stop bands in both low and high-frequency regions and widening it. Slesarenko [53] also have utilized curved elements considering Bezier splines to obtain diverse band gap structures. Our previous work [52] showed promising wave propagation characteristics compared to the regular hexagonal lattice by modifying the topology, introducing a combination of curved and straight beam elements in the unit cell. The curved elements result in local reflection and interference with the propagating wave, followed by the formation of new stop bands, thus changing the lattice's wave propagation behavior. Karlicic et al. [54] have explained the effect of added inertia on the regular hexagonal lattice to alter the dispersion behavior. Liu et al. [55] have introduced a square lattice with resonating beams to alter the band gap characteristics, obtaining extra stop bands in the low-frequency region. However, the results are insignificant regarding the number and width of the stop bands.

Following the previous works, we want to conceive lattices that could further control and manipulate wave propagation. The motivation of the work is how the wave propagation behavior can be influenced by keeping the same lattice base and the total area utilized by the corresponding conventional design. In this work, we propose a modified geometry consisting of a combination of curved and straight beams in the unit cell along with auxiliary straight cantilever beams at the nodes of the unit cell to obtain enhanced band gap behavior. The curved beams will act as a local scatterer apart from the scattering of the joints. To visualize it, we can think of a curved beam as an assembly of a straight beam, and the junctions will act as a scatterer. In contrast, extra nodal cantilevers further increase the amount of scattering. The scattered wave interferes with the propagating wave, and the destructive interference forms band gaps for a certain frequency. Due to the hexagonal base geometry, the reciprocal lattice is also the same as the conventional hexagonal lattice, and the IBZ is formulated according to the symmetry of the unit cell of the direct lattice. We have implemented finite element-based modeling considering straight Timoshenko beam elements to discretize the unit cell. The effect of different geometric parameters of the unit cell is explored. We have verified the occurrence of the band gap by comparing the band gap characteristics and transmissibility considering the commercial software COMSOL Multiphysics[2]. Today's additive manufacturing technologies allow us to

[2] Comsol Multiphysics®, https://www.comsol.com

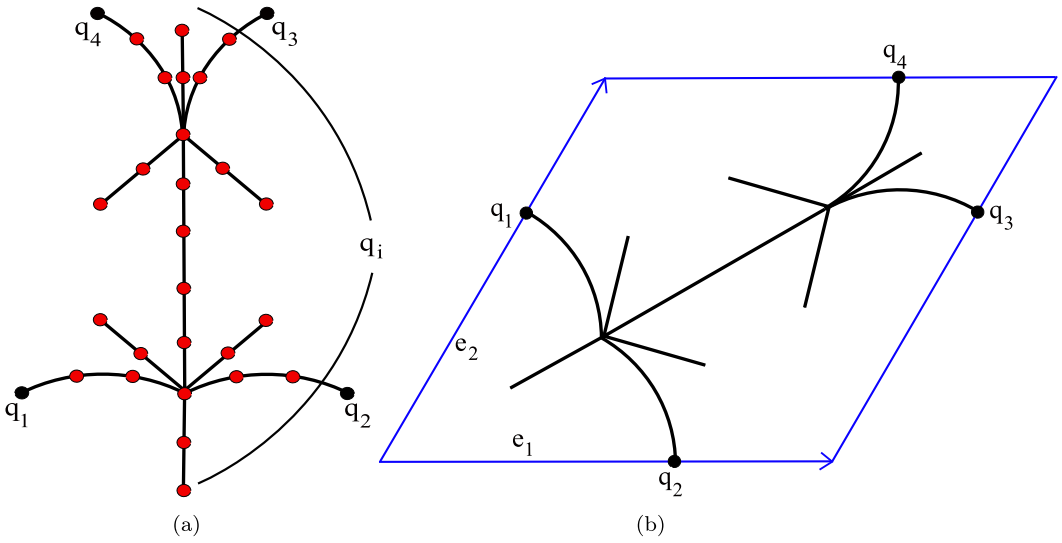

Fig. 2. (a) Finite element discretization of a unit cell. The required number of straight Timoshenko beam elements approximates the beams. q_1, q_2, q_3, and q_4 denote the boundary degrees of freedom and q_i denotes the internal degrees of freedom, and (b) a generic unit cell for a hybrid curved hexagonal lattice with shared degrees of freedom and with direct lattice vectors.

design lattices with various geometries, making lattices with complex and novel geometry to utilize in different engineering applications. The new hybrid lattice geometry gives insight into potential applications in mechanical filters, sound isolations, tunable acoustics, energy absorption, and control and manipulation of waves. The primary advantage lies in generating new lower and higher frequency band gaps by tuning the angles of curved beam elements and strategically placing additional beams while preserving the main topological features of the lattice.

2. Wave propagation in two-dimensional hybrid lattice

2.1. Geometry of the lattice and the unit cell

We propose a geometry that combines straight and curved beams and additional cantilever beams at the joints of the unit cell and call this lattice a hybrid lattice. The details of the new lattice geometry are shown in Fig. 1. The auxiliary short beams are inserted at the joints of the unit cell in a cantilever fashion. Introducing extra beams into the unit cell introduces two additional parameters capable of influencing the wave propagation behavior of the lattice: the length of the added beams and the inclination angle ϕ. Throughout this current study, the cell angle θ is set to 30°. The primary motivation is to investigate the impact of the extra beam and the combined effects of curved and extra beams. The lattice points of the conventional hexagonal lattice and the present lattice coincide, and the direct lattice vectors $\mathbf{e}_1$ and $\mathbf{e}_2$ are also the same for both cases. In this analysis, we consider ψ, ϕ, L_s, and L_v as the influencing parameters. Wave propagation characteristics are obtained by applying periodic boundary conditions to the unit cell through the Bloch theorem. Appendix A provides further details on the direct and reciprocal lattice vectors, while Appendix B offers a concise explanation of the Bloch theorem.

2.2. Timoshenko beam equations

We model the constituent beam members as assemblies of straight Timoshenko beams, incorporating the following material characteristics: ρ for density, t for beam thickness, E for modulus of elasticity, $G = E/(2(1+\nu))$ for shear modulus, and ν for Poisson's ratio. Additionally, we adopt the shear correction factor $k_s = 10(1+\nu)/(12+11\nu)$. The well-known governing equations for Timoshenko beams can be found in the literature [56]. However, we reiterate the derivation procedure based on Hamilton's principle for simplicity. Consequently, we define the variations of kinetic energy δK and potential energy δU.

$$\delta K = \int_0^L [\rho A \dot{u}\delta\dot{u} + \rho I \dot{\varphi}\delta\dot{\varphi} + \rho A \dot{w}\delta\dot{w}]\mathrm{d}x, \tag{1}$$

$$\delta U = \int_0^L \left[EA\frac{\partial u}{\partial x}\delta\frac{\partial u}{\partial x} + EI\frac{\partial \varphi}{\partial x}\delta\frac{\partial \varphi}{\partial x} + GAk_s\left(\varphi - \frac{\partial w}{\partial x}\right)\delta\left(\varphi - \frac{\partial w}{\partial x}\right)\right]\mathrm{d}x, \tag{2}$$

where δ denotes the variation operator and $w(x,t)$, $u(x,t)$, and $\varphi(x,t)$ represent the transverse displacement of the centroid, axial displacement of the centroid, and cross-sectional rotation, respectively. We adopt that $\dot{(\cdot)} \equiv \partial(\cdot)/\partial t$.

Using Eq. (1) and Eq. (2) and Hamilton's principle gives

$$\int_{t_1}^{t_2} (\delta K - \delta U)dt = 0. \tag{3}$$

Following the standard procedure, one can derive the governing equations for the longitudinal and transverse vibrations of the Timoshenko beam as:

$$\rho A\ddot{u} - EA\frac{\partial^2 u}{\partial x^2} = p(x,t), \tag{4}$$

$$\rho A\ddot{w} + GAk_s\left(\frac{\partial \varphi}{\partial x} - \frac{\partial^2 w}{\partial x^2}\right) = q(x,t), \tag{5}$$

$$EI\frac{\partial^2 \varphi}{\partial x^2} - GAk_s\left(\varphi - \frac{\partial w}{\partial x}\right) - \rho I\ddot{\varphi} = 0, \tag{6}$$

where $p(x,t)$ and $q(x,t)$ represents the external axial and transverse loads.

2.3. The finite element formulation of the unit cell

This section discusses implementing finite element analysis for the unit cell to acquire its dispersion properties. The constituent beams of the unit cell are discretized with straight Timoshenko beams. Each element has two nodes and three degrees of freedom (longitudinal displacement, transverse displacement, and rotation) associated with each node.

Finite element development is adopted from [57], where displacements $u(x,t)$ and $w(x,t)$ and rotation $\varphi(x,t)$ are approximated as follows

$$u(x,t) = \sum_{j=1}^{6} N_j^u(x)q_j(t), \quad w(x,t) = \sum_{j=1}^{6} N_j^w(x)q_j(t), \quad \varphi(x,t) = \sum_{j=1}^{6} N_j^\varphi(x)q_j(t), \tag{7}$$

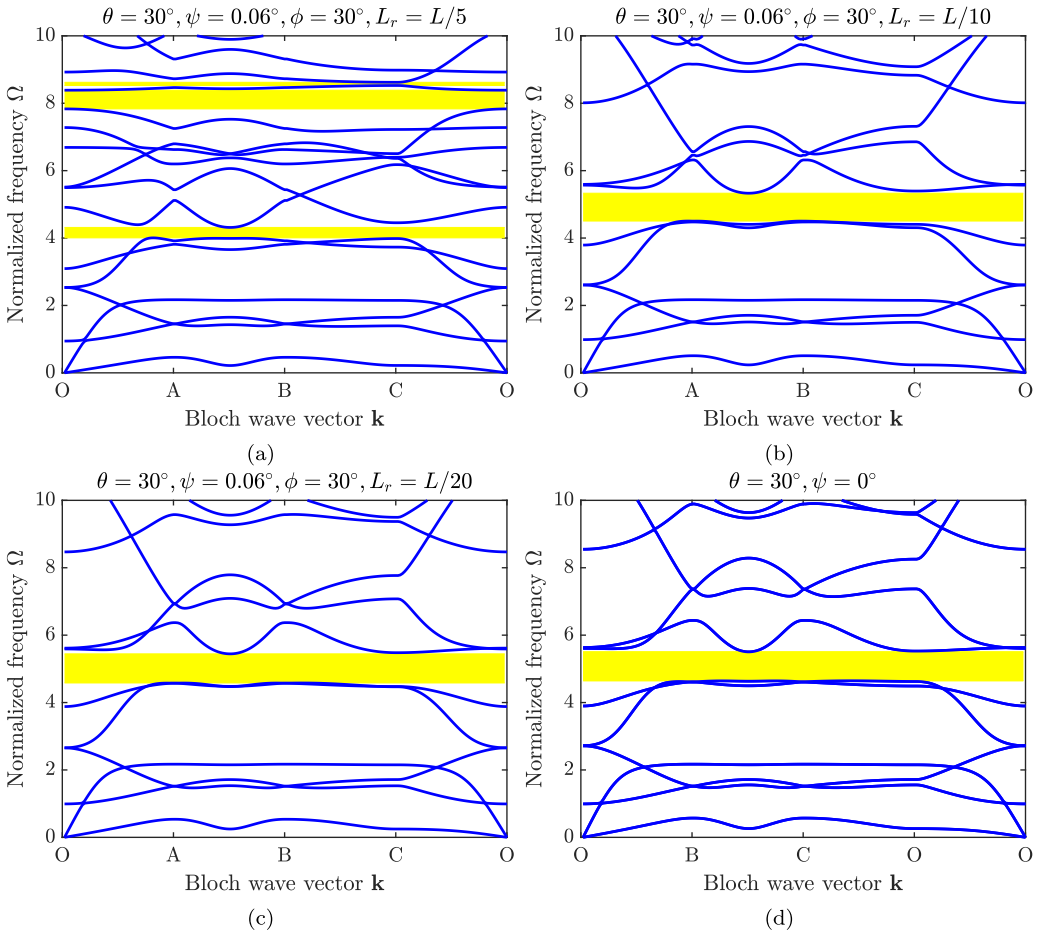

Fig. 3. Frequency band structures for lattice with $\theta = 30°$, $\psi = 0.06°$, $\phi = 30°$ and length of the additional beam (a) $L_r = L/5$ (b) $L_r = L/10$, (c) $L_r = L/20$, and (d) conventional hexagonal lattice with $\theta = 30°$ and $\psi = 0°$. θ, ψ, ϕ, and L_r are the cell angle, curvature angle, angle of the additional slant beams, and length of the additional beams, respectively. The results are obtained using Matlab.

with $N_j^u(x), N_j^w(x)$, and $N_j^\varphi(x)$, $(j = 1, 2, \ldots, 6)$ denoting the shape functions while the components of the nodal vector follow as $\mathbf{q}(t) = [u_1, w_1, \varphi_1, u_2, w_2, \varphi_2]^T$. The shape functions are mentioned in Appendix C. Considering the governing equations for a Timoshenko beam Eq. (4)–Eq. (6), energy variation Eq. (1)–Eq. (3) and approximation of displacements and rotation, cf. Eq. (7), we get

$$\mathbf{M}^e\ddot{\mathbf{q}}^e + \mathbf{K}^e\mathbf{q}^e = \mathbf{f}^e, \tag{8}$$

where $\mathbf{M}^e$ and $\mathbf{K}^e$ are the element mass and stiffness matrices, respectively, for the beam element while $\mathbf{q}^e$ represents the element displacement and $\mathbf{f}^e$ denotes force vector components. The local stiffness and mass matrices are assembled to obtain the global one with proper coordinate transformation

$$\mathbf{K} = \sum_{e=1}^{n_{ele}} \mathbf{K}_g^e, \quad \mathbf{M} = \sum_{e=1}^{n_{ele}} \mathbf{M}_g^e, \tag{9}$$

where $\mathbf{M}$ and $\mathbf{K}$ are the global mass and stiffness matrices of the unit cell and n_{ele} is a number of finite elements to discretize the unit cell. $\mathbf{K}_g^e$ and $\mathbf{M}_g^e$ are the globally transformed element stiffness and mass matrix, respectively. The matrix form of the equation of motion for the unit cell reads as follows

$$\mathbf{M}\ddot{\mathbf{q}} + \mathbf{K}\mathbf{q} = \mathbf{f}. \tag{10}$$

2.4. Dispersion relations for the periodic unit cell

The band gap characteristics are obtained by formulating an eigenvalue problem and considering periodic boundary conditions through the Bloch theorem. The solution of the eigenvalue problem will give us the dispersion surface, *i.e.* the relationship between the frequencies and the wavenumbers. First the harmonic solution $\mathbf{q}(x,t) = \mathbf{q}(x)e^{i\omega t}$ along with free wave propagation ($f = 0$) is considered for the equation of motion Eq. (10), which yields

$$(\mathbf{K} - \omega^2\mathbf{M})\mathbf{q} = \mathbf{0}, \tag{11}$$

where ω is the circular frequency of the free wave propagation and the nodal displacement vector $\mathbf{q}$ is considered as

$$\mathbf{q} = \{\mathbf{q}_1 \quad \mathbf{q}_2 \quad \mathbf{q}_3 \quad \mathbf{q}_4 \quad \mathbf{q}_i\}^T, \tag{12}$$

with $\mathbf{q}_1, \mathbf{q}_2$, $\mathbf{q}_3$, and $\mathbf{q}_4$ denoting the vectors of nodal displacements at unit cell nodes while $\mathbf{q}_i$ are degrees of freedom of internal nodes (see Fig. 2(a)). By employing Bloch's theorem and periodic boundary conditions at the nodes of a unit cell (see Fig. 2(b)) we obtain,

$$\mathbf{q}_3 = e^{k_1}\mathbf{q}_1, \quad \mathbf{q}_4 = e^{k_2}\mathbf{q}_2, \tag{13}$$

where k_1 and k_2 are the wavenumbers mentioned in Appendix B. The global nodal displacement vector can then be expressed by the following equation

$$\mathbf{q} = \mathbf{T}_b\mathbf{q}_r, \tag{14}$$

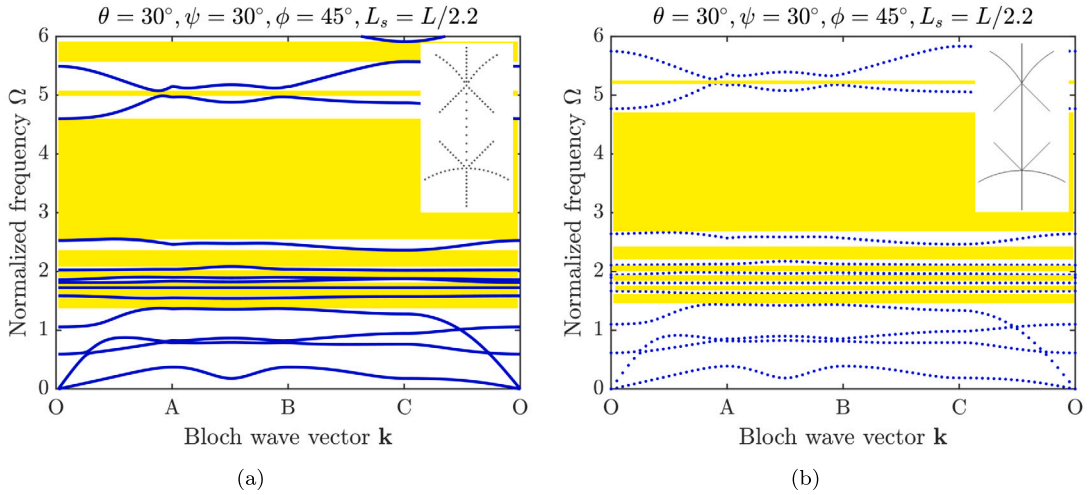

Fig. 4. Frequency band structures for lattice with $\theta = 30°$, $\psi = 30°$, $\phi = 45°$ and length of the additional beam $L_s = L_v = L/2.2$ obtained from (a) Matlab one-dimensional simulation with one-dimensional Matlab model on inset, and (b) COMSOL two-dimensional simulation with two-dimensional COMSOL model on inset. The slenderness ratio $\beta = t/L$ is 1/300.

Table 1
The boundary points of the irreducible Brillouin zone of hybrid hexagonal lattice for $\theta = 30°$.

IBZ boundary points	Hexagonal lattice $\theta = 30°$
O	$(0, 0)$
A	$(2\pi/3, -2\pi/3)$
B	$(4\pi/3, 2\pi/3)$
C	(π, π)

yielding the global vector of nodal displacements in the reduced form $\mathbf{q}_r = \{\mathbf{q}_0 \quad \mathbf{q}_i\}^T$ while the linear transformation matrix $\mathbf{T}_b$ is given as

$$\mathbf{T}_b = \begin{bmatrix} \mathbf{I} & \mathbf{0} & \mathbf{0} \\ \mathbf{I}e^{k_1} & \mathbf{0} & \mathbf{0} \\ \mathbf{0} & \mathbf{I} & \mathbf{0} \\ \mathbf{0} & \mathbf{I}e^{k_2} & \mathbf{0} \\ \mathbf{0} & \mathbf{0} & \mathbf{I} \end{bmatrix}. \tag{15}$$

By substituting Eq. (14) into Eq. (11) and pre-multiplying the results with the Hermitian (complex conjugate) transpose matrix $\mathbf{T}_b^H$ results in

$$(\mathbf{K}_r(k_1, k_2) - \omega^2 \mathbf{M}_r(k_1, k_2))\mathbf{q}_r = \mathbf{0}, \tag{16}$$

where the reduced mass and stiffness matrices are of the form

$$\mathbf{M}_r(k_1, k_2) = \mathbf{T}_b^H \mathbf{M} \mathbf{T}_b, \tag{17}$$

$$\mathbf{K}_r(k_1, k_2) = \mathbf{T}_b^H \mathbf{K} \mathbf{T}_b.$$

Solving the eigenvalue problem, cf. Eq. (16), involves considering a set of values for k_1 and k_2 within the first Brillouin zone to acquire dispersion surfaces $\omega = \omega(k_1, k_2)$. The dimension of the eigenvalue problem determines the number of dispersion surfaces. The geometry of the reciprocal lattice depends on the cell angle (θ) of the lattice, and the reciprocal lattice vectors ($\mathbf{e}_1^*, \mathbf{e}_2^*$) are obtained by following a standard procedure as explained in [58]. Appendix A mentions the direct and reciprocal lattice vectors and their schematic diagrams. The IBZ is derived by considering the symmetry property of the first Brillouin zone and the unit cell of the direct lattice. Focusing on wavenumber values that vary along the contours of the IBZ gives the two-dimensional plot of the dispersion. Table 1 shows the value of the contour points for the IBZ of the hexagonal lattice. Notably, the Brillouin zone for the regular hexagonal and the hybrid lattice remains the same.

3. Numerical study and discussion

This section conducts numerical investigations on the proposed hybrid curved hexagonal lattices (Fig. 1). This modification in architecture increases the number of geometric parameters that influence wave propagation characteristics. Besides the cell angle θ, other parameters include the curvature angle ψ, individual lengths of the additional beams L_s and L_v, and the inclination angle of the auxiliary beam members ϕ. We have investigated the impact of the curvature angle ψ in our earlier work [52], revealing the occurrence of both low and high-frequency stop bands. In this study, the additional parameters from added beams and the combined influence of the curvature angle are leveraged, enriching the band gap characteristics. MATLAB is employed to write finite element codes and apply the Bloch theorem for periodic analysis to obtain the dispersion diagram. We have used 30 finite elements for the discretization of the curved beam and the same number of elements for other constituent beam members. The number of elements is adopted from our previous work [52]. Where the number was fixed by performing some convergence analysis. To verify the finite element results using a finite lattice, we employ COMSOL.

We perform dispersion analysis by adjusting the wave vector ($\mathbf{k}$) varying along the contour $O-A-B-C-O$ (Fig. A.1). The material parameters considered in this work are adopted from Karlicic et al. [54]. The properties are: elastic modulus $E = 210\,\text{GPa}$, mass density $\rho = 25 \times 10^3\ \text{kg/m}^3$, Poisson's ratio $\nu = 0.25$. The geometric parameters include a slenderness ratio $\beta = t/L = 1/15$ and a beam length of $L = 0.125\,\text{m}$ (Fig. 1(b)). The length of the added vertical and slant beam members are denoted as L_v and L_s, respectively. Whereas, if the length of both beams is the same, then the length of both beams is termed as L_r in the manuscript. We normalize the frequencies (ω), obtained by solving the eigenvalue problem, with $\omega_0 = \pi^2/L^2\sqrt{EI/\rho A}$, representing the first flexural natural frequency of the simply-supported beam. The other geometric parameters are the second moment of inertia $I = bt^3/12$ and the area $A = bt$ (b is the width and t is the thickness of the beam). The following sections discuss the effect of the added beams' length, inclination angle, and the curvature angle's combined effect on the proposed lattice's wave propagation behavior. In this study, we maintain the cell angle θ value at 30° for all cases.

3.1. Validation of band structures

To validate the numerical code, we obtain the band gap characteristics for a small curvature angle and shorter lengths of additional beam members, comparing them with the conventional hexagonal lattice. As

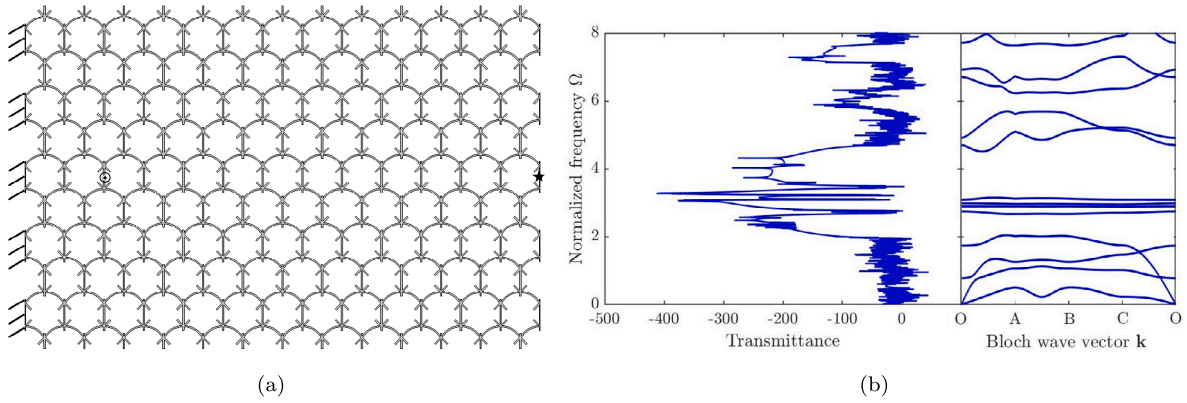

Fig. 5. Schematic diagram of (a) the finite hybrid curved hexagonal lattice with boundary condition; ★ denotes the excitation point and ⊙ denotes the measuring point, and (b) transmittance and the frequency band structures of the corresponding unit cell with $\theta = 30°$, and $\psi = 30°$, $\phi = 45°$, length of additional beam members: vertical $L_v = L/5$, and slant $L_s = L/2.5$.

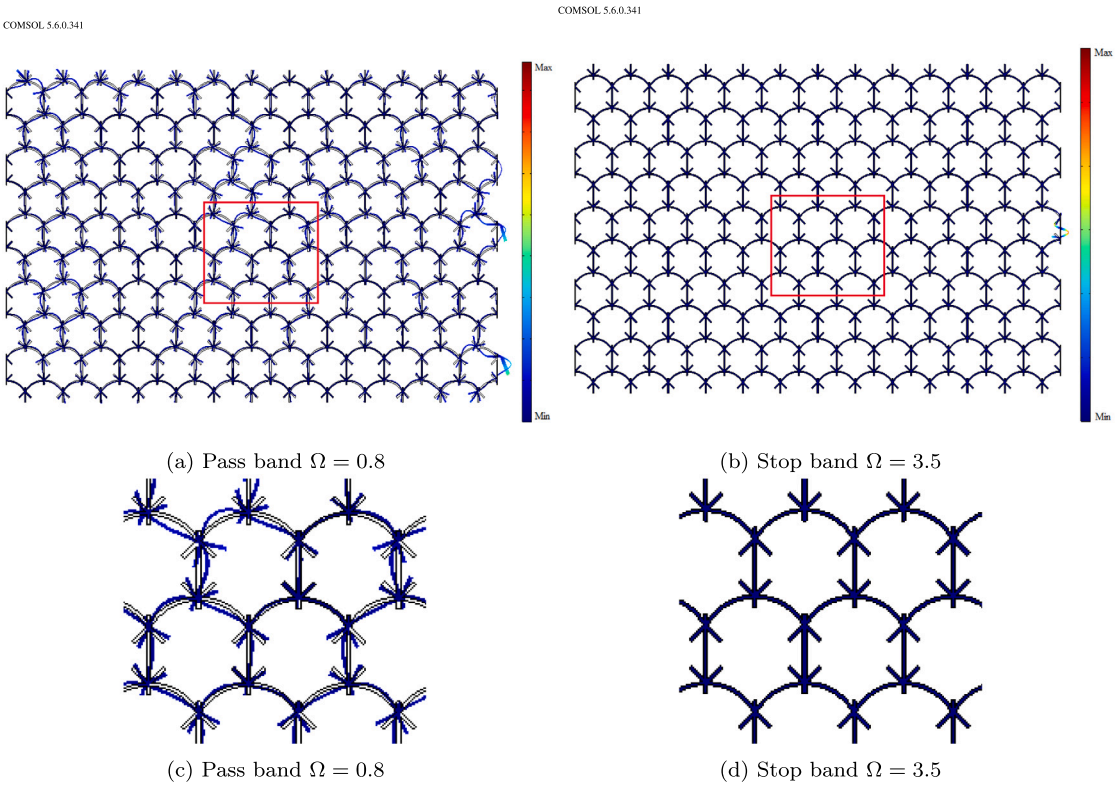

Fig. 6. Deformation of a finite lattice subjected to harmonic excitation along x direction for normalized frequency (a) $\Omega = 0.8$ (pass band) and (b) $\Omega = 3.5$ (stop band) with the region of interest shown in a red box. The magnified region of interest corresponds to (c) $\Omega = 0.8$ (pass band) and (d) $\Omega = 3.5$ (stop band). The geometric details of the unit cell for the lattice are: $\theta = 30°$, and $\psi = 30°$, $\phi = 45°$, length of additional beam members: vertical $L_v = L/5$, and slant $L_s = L/2.5$.

we decrease the curvature angle and lengths of the additional beams, we observe that the band gap diagram converges to the conventional hexagonal one ($\theta = 30°$). The dispersion plots for the regular hexagonal lattice are available in previous works [22,52]. The convergence of the dispersion plots for the hybrid curved hexagonal lattices toward the conventional one is illustrated in Fig. 3. Furthermore, we compare the dispersion diagram obtained from MATLAB with that obtained from COMSOL analysis (Fig. 4). One can observe that the characteristics match precisely with each other except the location of the stop bands. This is due to different modeling techniques used for the finite element analysis. We use one-dimensional modeling in MATLAB code, whereas COMSOL uses two-dimensional finite elements for analysis. The number of elements for each beam is approximately fixed as 1250 by following an iterative approach. We fix the number of elements by varying the number of triangular elements across the width of the beam from 2 to 5. It showed that the band diagrams are the same for all the cases for the frequency range of interest. So, we finally used two elements per width to run the simulation. We have used the triangular Lagrange element and user-defined meshing option in COMSOL. The next section consists of COMSOL-based two-dimensional finite element verification for the band diagram.

3.2. Finite element verification of band-gap characteristics with finite lattice

This section deals with the finite element verification of the band structure by considering a finite lattice. The unit cell of the lattice

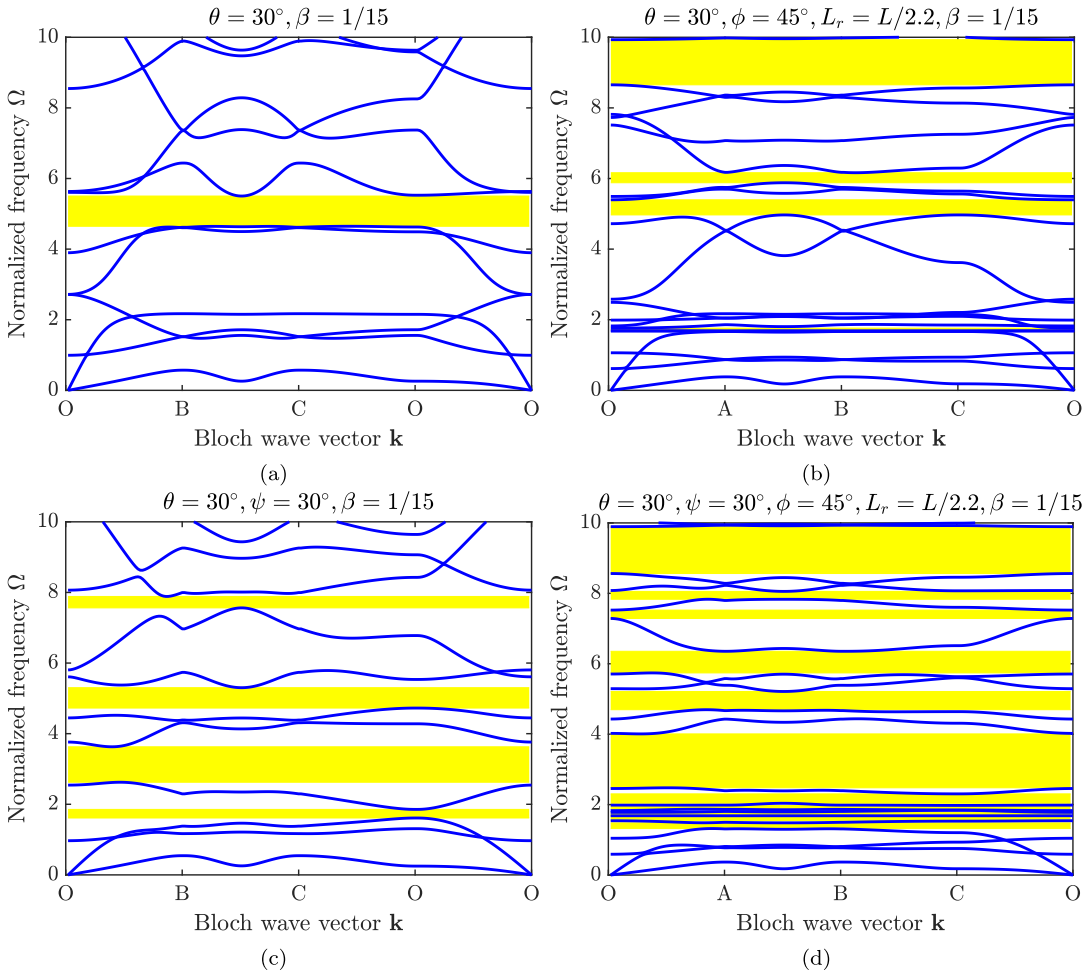

Fig. 7. Frequency band structures of the (a) conventional hexagonal lattice with $\theta = 30°$, (b) conventional hexagonal lattice with additional beam members with $\phi = 45°$ and length $L_r = L/2.2$, (c) curved hexagonal lattice with $\theta = 30°$ and $\psi = 30°$, and (d) hybrid hexagonal lattice with $\theta = 30°$, $\psi = 30°$, $\phi = 45°$, and $L_r = L/2.2$, and (d) evolution of the frequency band-gaps with reverse curvature angle Ψ considering cell angle The slenderness ratio ($\beta = t/L$) is 1/15 for all the cases. L is the length of the main constituent beam.

structure features the following geometric configurations: $\theta = 30°$, $\psi = 30°$, $\phi = 45°$, and lengths of additional beam members — vertical ($L_v = L/5$) and slant ($L_s = L/2.5$). The left boundary of the lattice is subject to a fixed boundary condition, and excitation is applied on the right-hand side, as depicted in Fig. 5(a). The geometry of the two-dimensional lattice is created in Solidworks and exported as DXF file to create the geometry in COMSOL. Finally, we perform the frequency domain analysis in COMSOL and derive the transmittance plot (Fig. 5(b)) by examining the frequency responses of both the excitation and the measuring point. The excitation is applied in the x-direction, and the transmittance (TR) is calculated as

$$TR = 20 \log_{10} \frac{u_{mes}}{u_{exc}}, \tag{18}$$

where u_{mes} and u_{exc} represent the displacements of the measuring and excitation points, respectively. We compare the transmittance for the finite lattice with the band gap characteristics of the same unit cell obtained from the periodic analysis, as shown in Fig. 5(b). It is important to note that two-dimensional elements are employed for finite element modeling to obtain the transmittance for the finite lattice. The band gap characteristics are also obtained in COMSOL, considering two-dimensional elements for finite element-based Bloch analysis. A notable observation is that the location of the band gaps in the transmittance plot and the dispersion diagram align well. The transmittance decreases as we shift the measuring point further from the excitation point. In the following sections, we obtain the results for the parametric influences on the dispersion behavior from our developed finite element codes in MATLAB.

Next, two deformation diagrams (see Fig. 6) are plotted to observe the finite lattice's wave attenuation at different excitation frequencies. Fig. 6(a) illustrates the steady-state response of the finite lattice corresponding to the excitation frequency in the pass band ($\Omega = 0.8$), while Fig. 6(b) shows the same for frequency value from the stop band ($\Omega = 3.5$). The unit cell of the lattice has the following geometric details $\theta = 30°$, $\psi = 30°$, $\phi = 45°$, length of additional beam members: vertical $L_v = L/5$, and slant $L_s = L/2.5$. The analysis is conducted in COMSOL, and the deformation values are scaled with the same factor for both cases. Observations from the plots reveal that the lattice experiences relatively more deformation for excitation in the pass band than in the stop band, where no deformation occurs far from the excitation point.

3.3. Effect of different geometric parameters on the band gap characteristics

This section deals with the effect of different geometric parameters of the unit cell on the band gap characteristics of the hybrid lattice. Mainly, the impact of the additional beam members' length and inclination angle is investigated along with the combined effect of the curvature angle. The combined effect of the curvature angle and the geometric parameters of the additional beam plays a significant role in influencing the band gap characteristics. An investigation is performed considering the effect of only the additional beam on the conventional lattice and on the curved lattice with curvature angle

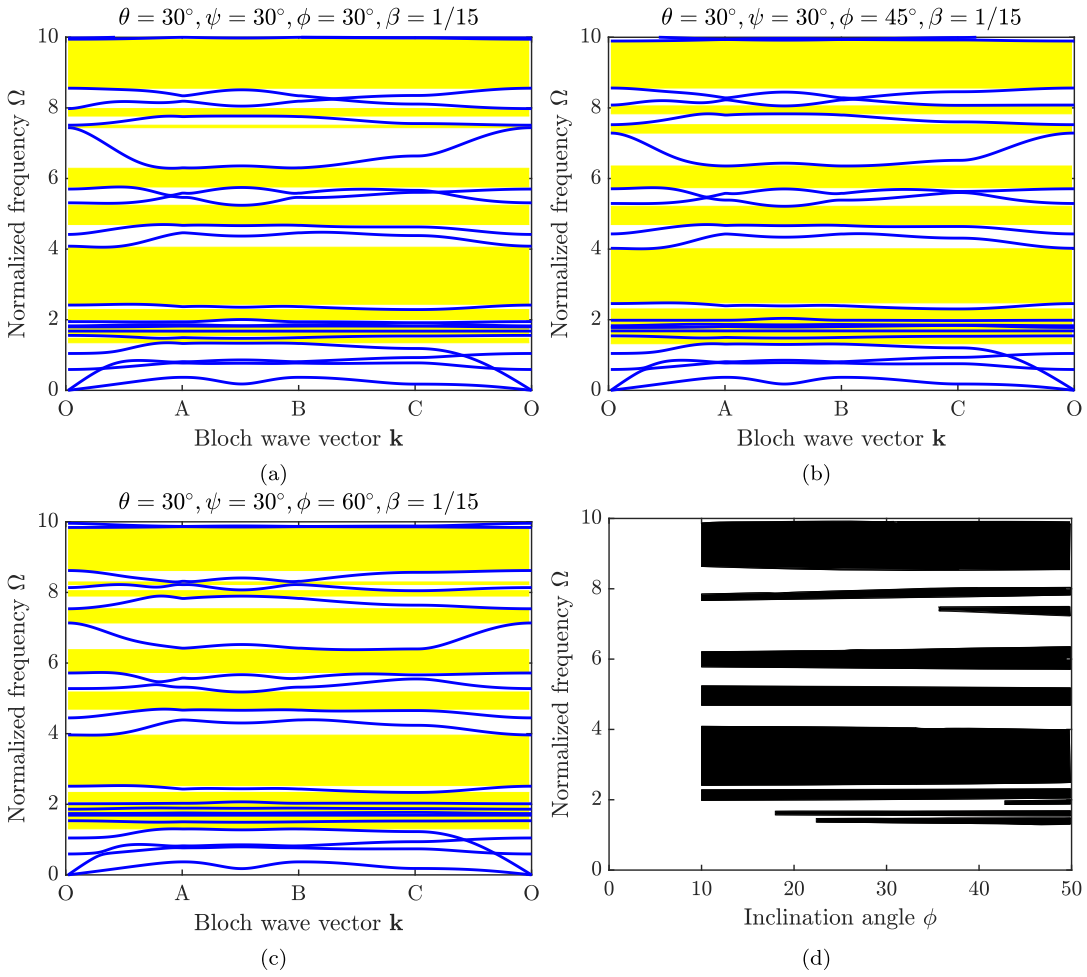

Fig. 8. Frequency band structures of the hybrid lattice with $\theta = 30°$, $\psi = 30°$ $L_r = L/2.2$ and (a) $\phi = 30°$, (b) $\phi = 45°$, (c) $\phi = 60°$, and (d) evolution of the frequency band-gaps with inclination angle of the nodal cantilever beam ϕ considering cell angle $\theta = 30°$. The slenderness ratio ($\beta = t/L$) is 1/15 for all the cases. L is the length of the main constituent beam.

$\psi = 30°$ (Fig. 7). We can observe that the band gap characteristics for the conventional lattice (Fig. 7(a)) are changing due to the inclusion of additional beams at the joints (Fig. 7(b)). Modes are compressed in the lower frequency zone near $\Omega = 2$, and new band gaps are forming in the higher frequency region. However, the characteristic is not promising in forming new stop bands, especially at the lower frequency region. It is evident from Fig. 7 that new band gaps can be formed both in the lower and high-frequency region by changing the architecture of the unit cell from the assembly of the straight beam to a combination of both straight and curved beam. However, the combined effect of both curvature angles and the inclusion of extra beam members at the joints influence the dispersion behavior and generate wider band gaps in both low and high-frequency regions. We observe increased band gaps between $\Omega = 2$ and 4 (Fig. 7(c) and Fig. 7(d)), and there are several small band gaps occurred below $\Omega = 2$. Also, We observe increased band gaps around $\Omega = 6$ (Fig. 7(b) and Fig. 7(d)), and two more stop bands appeared near $\Omega = 8$. So, the combined effect of the curvature angle ψ and the extra beam members could be utilized for wave attenuation problems. The next sections explore the hybrid lattice's capability in the vibration reduction domain.

3.3.1. Effect of inclination angle of the additional beams on the band-gaps

The effect of the inclination angle ϕ of the additional beam member is explored by increasing the ϕ value for the hybrid lattice through, and Fig. 8 shows it. The values of the cell angle θ, curvature angle ψ, and the length of the additional beam L_r are 30°, 30°, and $L_r = L/2.2$, respectively. The effect of the inclination angle ϕ is not that significant on the dispersion characteristics. However, for a higher value of ϕ, the band gaps between $\Omega = 4$ to 8 are changing. The width of the stop band near $\Omega = 8$ is increasing a little with ϕ if we observe the plots. In comparison, the low-frequency characteristics remain almost unchanged. The influence of the inclination angle is clear from the evolution plot Fig. 8(d). Though the impact is not much, there is still formation of new band gaps near the normalized frequency value of 2 and 7.5 for higher values of inclination angle.

3.3.2. Effect of length of the additional beams

This section deals with the effect of the additional beam members' length on the hybrid lattice's dispersion characteristics. Fig. 9 shows how the length of the additional beam members (L_r) influence the characteristics. The L_r value is kept the same for vertical and slant beam members. It can be observed that for a beam with a smaller length, the dispersion diagram (see Fig. 9(a)) is close to the dispersion diagram of the curved lattice without the extra beams (curved lattice with $\theta = 30°, \psi = 30°$ [52]). A new stop band is opening near $\Omega = 4$. For the next case with $L_r = L/7$, the stop bands have shifted towards the lower frequency regions, and high-frequency stop bands appear near $\Omega = 10$. The band gap characteristics change drastically as we increase the L_r value. For $L_r = L/3$, several low-frequency stop bands are formed, and modes are pushed toward the low-frequency region.

The evolution plot Fig. 9(d) shows the impact of the length of the additional beam members on the dispersion behavior. The plot depicts

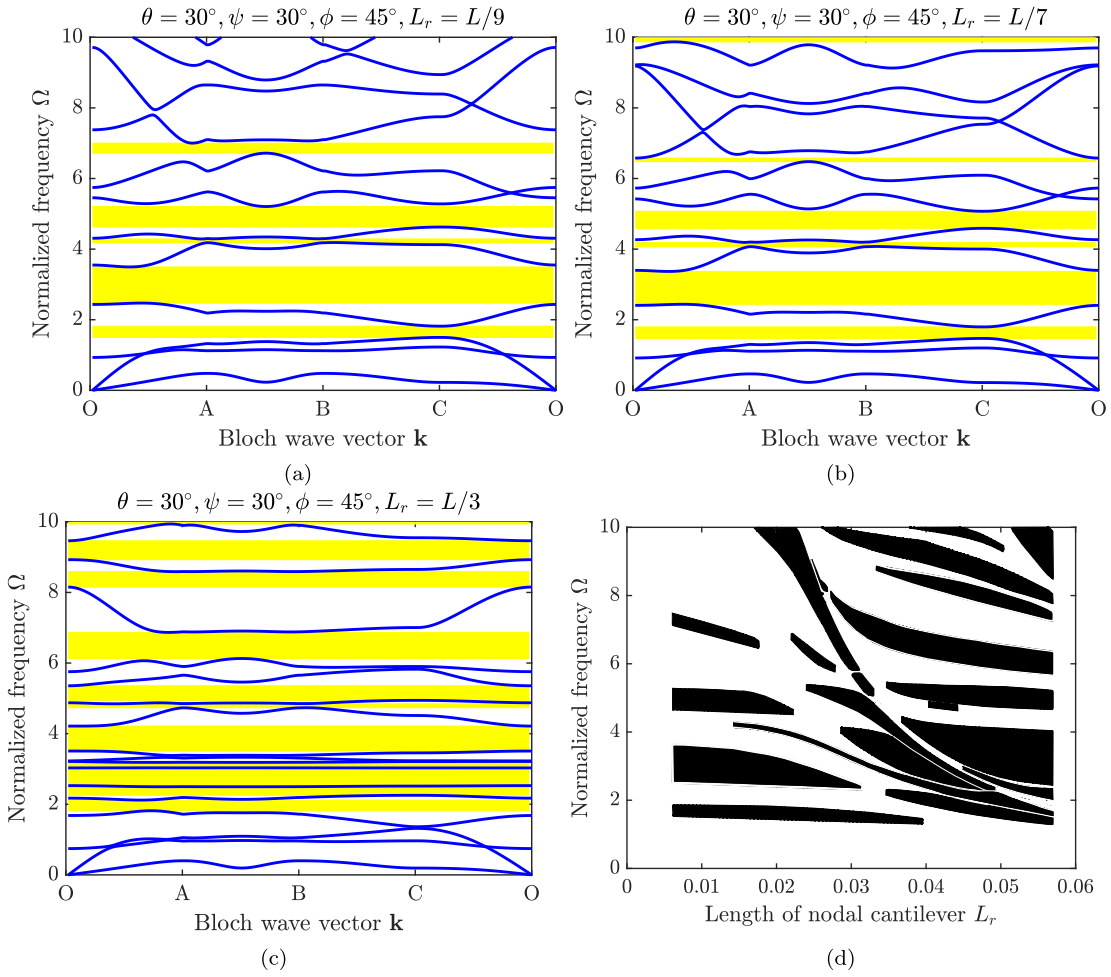

Fig. 9. Frequency band structures of the hybrid lattice with $\theta = 30°$, $\psi = 30°$ $\phi = 30°$ for (a) $L_r = L/9 \approx 0.014$ m, (b) $L_r = L/7 \approx 0.018$ m, (c) $L_r = L/3 \approx 0.042$ m, and (d) evolution of the frequency band-gaps with the length of the nodal cantilevers (L_r). Plot (a)–(c) corresponds to a specific value of $L_r = L/9$, $L/7$, and $L/3$ in the evolution plot, respectively. The slenderness ratio ($\beta = t/L$) is 1/15 for all the cases. L is the length of the main constituent beam.

the nature of the lattice without the nodal cantilevers when the L_r value is less. The band gaps are Bragg type when the L_r value is less. As the L_r takes higher values, the Bragg band gaps disappear completely, and new band gaps form after that. The disappearance of existing band gaps and the formation of new ones at the first stage might be due to the effect of the vibration of the nodal cantilevers with the increasing L_r value. The combined nature of the disappearance of band gaps and the occurrence of new band gaps and their shifting towards the lower frequency region supports the phenomenon of compression of the frequency band curves. This trend is evident from the individual plots of the dispersion diagram considering different L_r values. The band gaps originating between $L_r = 0.02 - 0.04$ shift faster to the lower frequency region. One can notice the shifting of band gaps towards the lower frequency region for higher values of L_r (*e.g.*, L_r value 0.04–0.058) as well, and the width of the band gaps also increases for almost all the band gaps in that zone. The interaction of the curved beam and nodal cantilevers is prominent in the large values of L_r. The band gap characteristics are complex in this case. Next, the effect of the different lengths for the vertical and slant additional beams is investigated. For that, the length of the vertical added beams is fixed to $L_v = L/5$, and the length slant of extra beams (L_s) is varied and vice versa. The effect of L_s is shown in Fig. 10. When the L_s value gets higher than the L_v number of stop bands, their width gets bigger for the major stop bands, and they also shift to the lower frequency region (see Fig. 10(c) and Fig. 10(d)). We can also observe that near $\Omega = 2.5$, the modes get compressed, and there are a few flat bands in this region. It is also clear from Fig. 10(d) that the nature of the plot is similar to Fig. 9(d). The nodal cantilevers have some influence in creating the new band gaps in the mid-region (L_s value 0.02–0.04), and the interaction of the curved beam and nodal cantilevers also creates new band gaps for higher values of L_s followed by increasing of their width.

The band gaps follow a different trend, unlike the previous cases where L_v is changed, keeping L_s to a fixed value (Fig. 11). Two lower frequency band gaps do not disappear. Instead, it continues. Like in earlier cases, a few new band gaps are formed for the L_s value, around 0.02-0.04. Most of the dispersion curves can be separated visually. The stop bands shift towards the lower frequencies and widen (Fig. 11(d)). One can notice from the plots (Figs. 9–11) that an almost perfect flat band is occurring for a more significant length of the auxiliary beam members ($L_r \geq L/3$) at that frequency range of interest. The 6th mode in the dispersion plot corresponds to a flat band for the lattice with $L_r = L/2.2$ (Fig. 8). That means there is no energy transfer due to a zero group velocity, and the vibration is confined to the auxiliary beams. Majorly, the auxiliary slant beams vibrate in their first mode at the frequency value corresponding to the observed flat band. Further, Fig. 8 has a few nearly flat bands and a couple of stop bands up and down to them. The stop bands adjacent to the almost perfect flat band might emerge due to the local resonance itself or the combined effect of local resonance and Bragg scattering. The almost flat conducting bands corresponds to the vibration confined to the nodal cantilevers

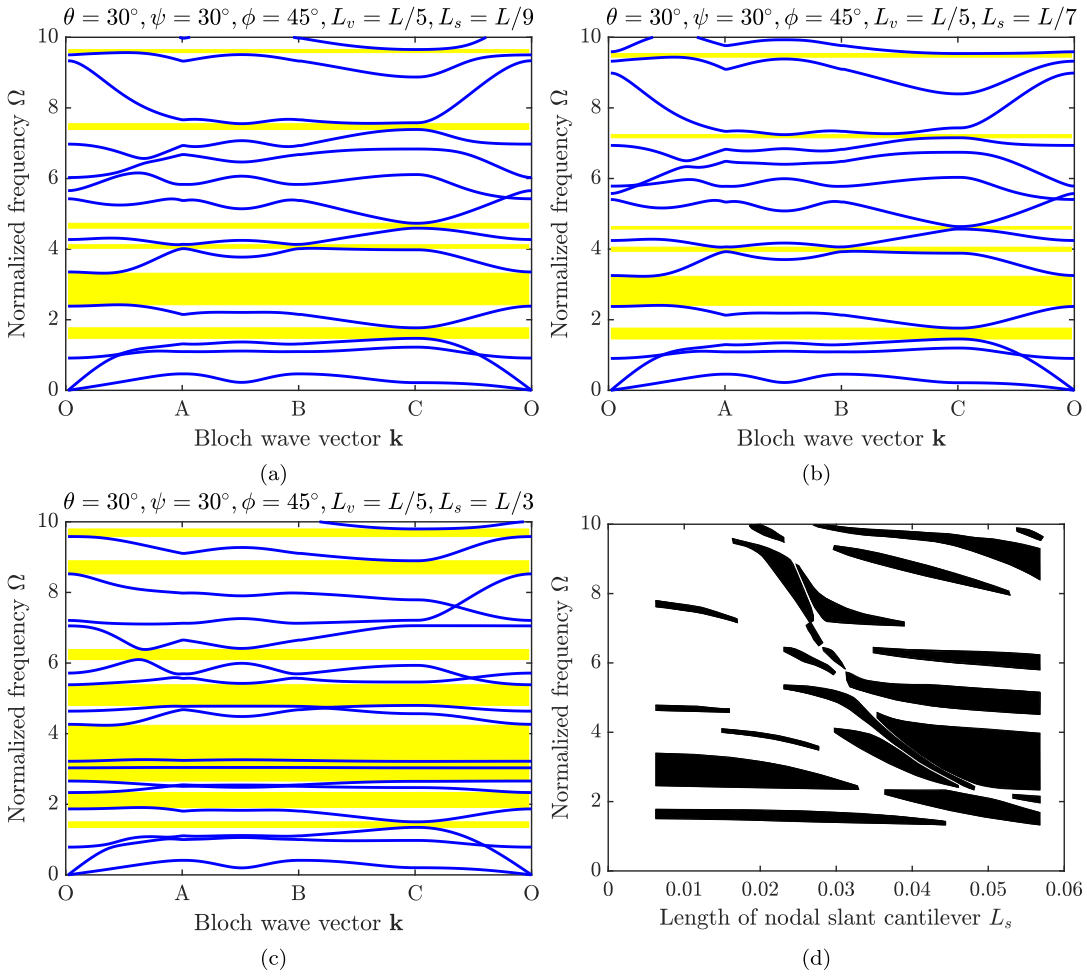

Fig. 10. Frequency band structures of the hybrid lattice with $\theta = 30°$, $\psi = 30°$ $\phi = 45°$, $L_v = L/5$ for (a) $L_s = L/9 \approx 0.014$ m, (b) $L_s = L/7 \approx 0.018$ m, (c) $L_s = L/3 \approx 0.042$ m, and (d) evolution of the frequency band-gaps with varied length of slant beam. Plot (a)–(c) corresponds to a specific value of $L_s = L/9$, $L/7$, and $L/3$ in the evolution plot, respectively. The slenderness ratio ($\beta = t/L$) is 1/15 for all the cases. L is the length of the main constituent beam.

mostly. It is worth mentioning that these narrow conducting bands do not significantly affect the attenuation capabilities of nearby band gaps occurring at the corresponding frequency ranges, thus showing their potential for wave energy absorption.

We can observe the individual effect of the vertical and slant beam members on the dispersion behavior from Fig. 12. The dispersion characteristics for lattice with only slant beams with $\phi = 45°$ and $L_s = L/2.2$ are shown in Figs. 12(a) and 12(b) shows the same considering only the vertical beam with $L_v = L/2.2$. From the plots, it is evident that both additional beams influence the same band gaps. The width of the stop band occurring near $\Omega = 3$ is higher for the case with slant members. The higher frequency band near $\Omega = 7$ is wider for the case with the vertical beam. Considering both vertical and slant extra beams allows appropriately tuning the band gap characteristics to meet the design purpose.

Another case has been studied varying the curvature angle and keeping $L_v = L/5$, $L_s = L/2.5$, and $\phi = 60°$. The plots in Fig. 13 show the effect of the curvature angle on the dispersion behavior in the presence of additional beam members. It is clear from the plot that due to the increase in the curvature angle ψ, the width of the band gaps is increasing for most of them, and their numbers are also increasing while shifting towards the lower frequency region. To obtain the detailed picture, we potted the evolution of the band gap (Fig. 13(d)) by continuously varying the curvature angle ψ. It shows that the increase in the width of the band gaps is not monotonic for all the gaps. The change varies for specific gaps, but all the gaps shift towards the lower frequency region with increasing ψ value. We can also observe from the results that the band gap characteristics are more diverse if the length of the slant beam (L_s) is more than the length of the vertical nodal cantilever (L_v). We have omitted the smaller band gaps in the evolution plots. This observation can be utilized in the future for inverse design problems. If we notice the dispersion behavior, one can find that the slope of the dispersion curves for the long wavelength case is decreasing. That is, the group velocity for both longitudinal and shear waves is getting reduced. This phenomenon will be observed in the next section, where the iso-frequency contours are discussed.

3.4. The iso-frequency contours

This section discusses the iso-frequency contours of the hybrid lattice. These contours are obtained from dispersion surfaces (*e.g.* see Alomar and Concli [12]), where the group velocity direction is perpendicular to it. At the same time, its magnitude is related to the closeness of two successive lines. Though group velocity and its direction can be easily and explicitly calculated from the iso-frequency contour analysis, the discrete nature of these contours results in frequency overlapping between different modes, which requires consideration of all dispersion surfaces in the frequency band of interest. Therefore, in [59], Zelhofer and Kochmann have suggested another approach based on

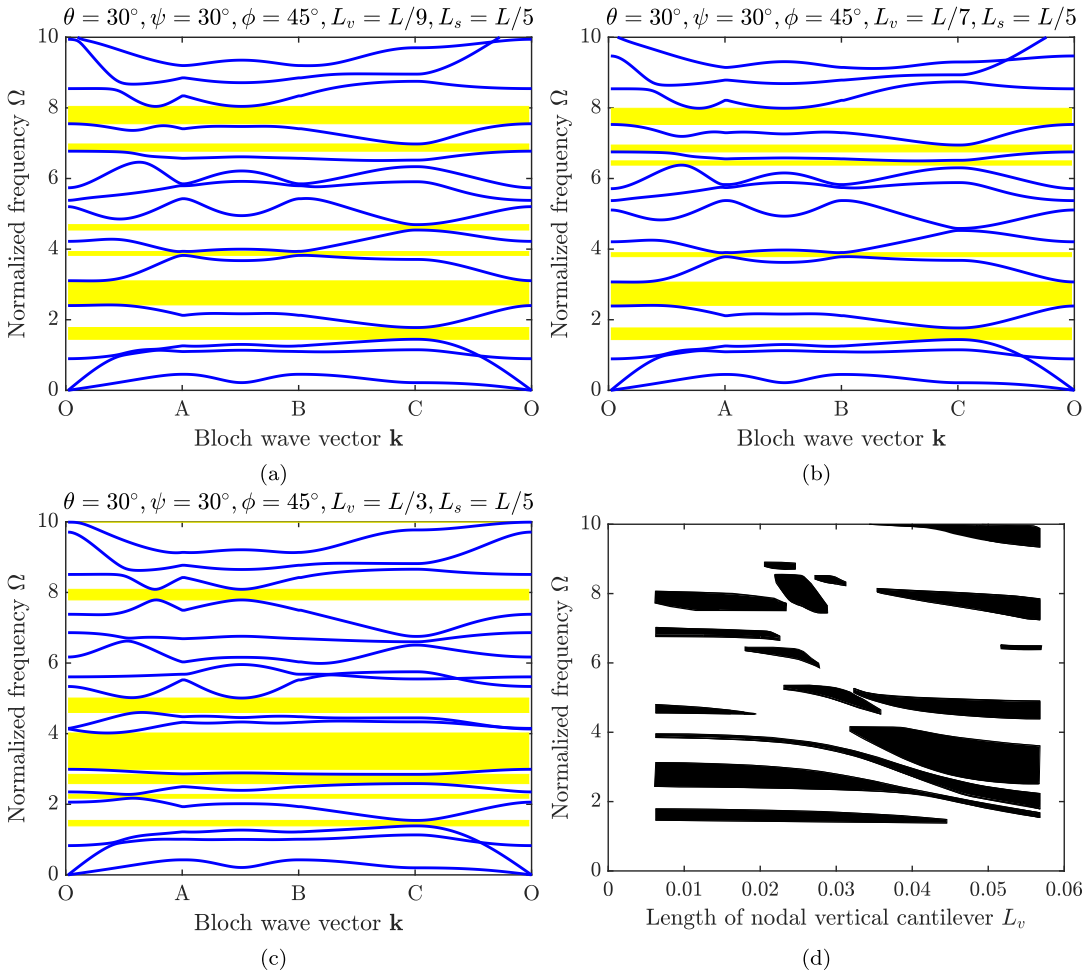

Fig. 11. Frequency band structures of the hybrid lattice with $\theta = 30°$, $\psi = 30°$, $\phi = 45°$, $L_s = L/5$ for (a) $L_v = L/9 \approx 0.014$ m, (b) $L_v = L/7 \approx 0.018$ m, (c) $L_v = L/3 \approx 0.042$ m, and (d) evolution of the frequency band-gaps with varied length of vertical nodal cantilever. Plot (a)–(c) corresponds to a specific value of $L_v = L/9$, $L/7$, and $L/3$ in the evolution plot, respectively. The slenderness ratio ($\beta = t/L$) is 1/15 for all the cases. L is the length of the main constituent beam.

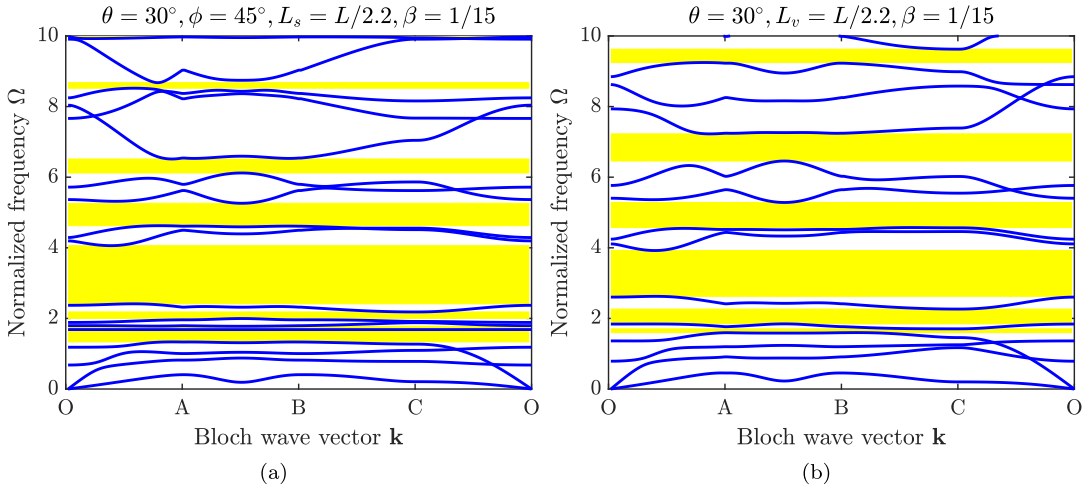

Fig. 12. Frequency band structures of the hybrid lattice with $\theta = 30°$, $\psi = 30°$ and considering only (a) additional slant beams with $L_s = L/2.2$ and $\phi = 45°$ and (b) vertical additional beam with $L_v = L/2.2$. The slenderness ratio ($\beta = t/L$) is 1/15 for all the cases. L is the length of the main constituent beam.

direct interpolating dispersion surfaces whose differentiation results in continuous group velocity in the momentum space. Here, the analysis is limited to the observation of iso-frequency contours of the first four modes, giving enough information about the directionality of wave propagation in the frequency range of interest, while a more detailed analysis is out of the scope of this study. In the case of observed lattice structures, the iso-frequency contours can obtain complex shapes. We can observe the comparison of the iso-frequency contours among the regular hexagonal, curved hexagonal, and hybrid lattice in Fig. 14 considering the first four modes. The plots for mode I reveal that

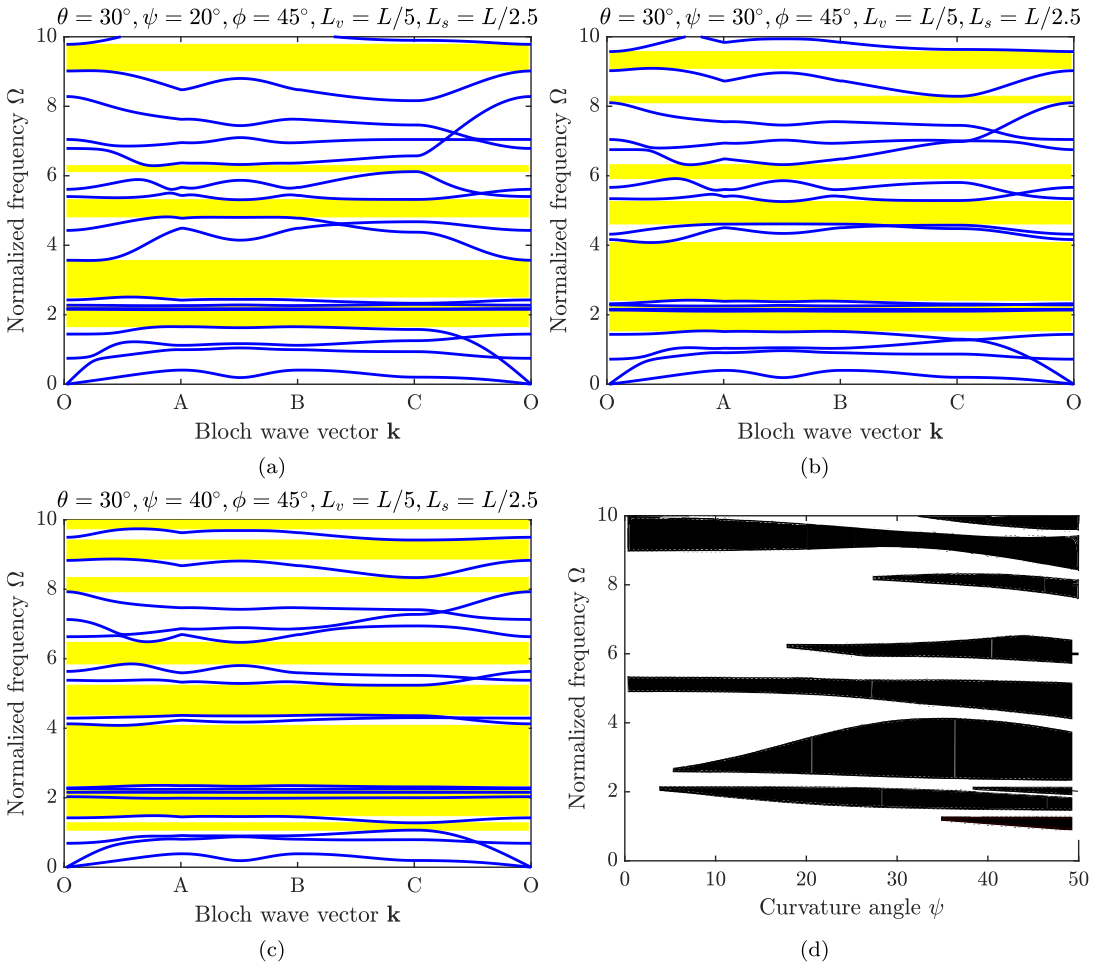

Fig. 13. Frequency band structures of the hybrid lattice with $\theta = 30°$, $\phi = 45°$, $L_s = L/2.5$, $L_v = L/5$ for (a) $\psi = 20°$, (b) $\psi = 30°$, (c) $\psi = 40°$, and (d) evolution of the frequency band-gaps with curvature angle ψ. Plot (a)–(c) corresponds to a specific value of $\psi = 20°$, $\psi = 30°$, and $\psi = 40°$ in the evolution plot, respectively. The slenderness ratio ($\beta = t/L$) is 1/15 for all the cases. L is the length of the main constituent beam.

the contours are almost circular for long wavelength limits (low frequencies) for all considered lattice types. Moreover, the low-frequency iso-frequency contours are spaced in nearly concentric circles, revealing the uniform propagating wavefront in all directions, similar to those in the isotropic homogeneous body. One can observe that the contours are closely spaced for conventional hexagonal lattices, thus having a higher wave speed than the other lattices. It is the hybrid lattice whose wave speed is the lowest as there are fewer numbers of contours and they are widely spaced. For even higher frequencies, the iso-frequency contours undergo topological disconnection, indicating the existence of directional band gaps. Moreover, the length of contours decreases towards the higher frequencies until they disappear at the edges of the IBZ. If we consider higher modes, the nature of the contours becomes more complex. The lobed nature of the contours shows the anisotropic behavior of the lattices at those frequency values, which means that the wave beaming response will occur in the lattice for the corresponding harmonic force point excitation, as reported in the literature for similar lattice types [59]. The contours are closely packed in the lower frequency region for mode II and low in density towards the edge of the Brillouin zone, corresponding to a flat dispersion surface. The dispersion behavior of the hybrid lattice for modes II and III is more complex than the other two cases.

4. Summary and conclusions

This work presents the wave propagation characteristics of a hybrid curved hexagonal lattice. Incorporating the curved and additional beam elements results in diverse band gap characteristics while keeping the total area for the lattice constant. The effect of the geometric parameters of the additional beam members and the combined effect of the curvature angle of the curved constituent beams are investigated. The key findings are as follows:

- The length of the additional beams plays an important role in creating new band gaps. For longer lengths of the additional beams, the number of gaps increases. But it is not monotonic. The evolution plots depicts the clear picture of the band gap characteristics. The effect of length of the nodal cantilevers and different lengths of the vertical and slant nodal beams has complex behavior. The diverse band characteristics can be utilized further for design purposes. The emergence of multiple flat bands within the low and high-frequency ranges also occurs, indicating their nearly zero group velocity and confinement of wave modes solely to the attached auxiliary slant beams.
- The orientation angle of the additional slant beams does not significantly affect the dispersion behavior compared to the length variation of the additional beams.
- The combined effect of the curvature angle and the length of the additional slant beams have a significant influence in generating new stop bands and increasing and decreasing the width of the stop bands in all frequency ranges.
- Including additional beams decreases the wave speed for the longitudinal wave and delivers diverse directional behavior for high-frequency modes. The findings from the present investigations

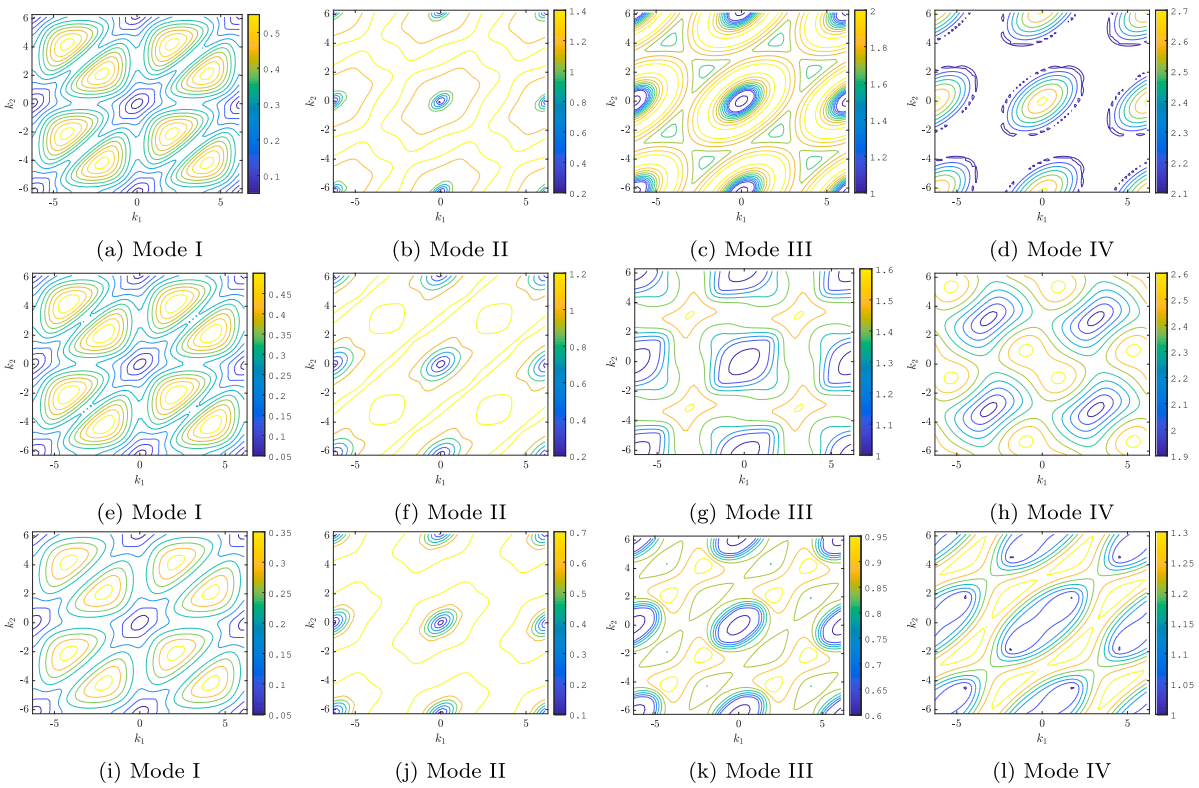

Fig. 14. Iso-frequency contour plots for the first four modes of the conventional, curved hexagonal lattice and hybrid curved hexagonal lattice. The first row shows the contours for hexagonal lattice with straight constituent beams with $\theta = 30°$. The second row shows the contour for the curved hexagonal lattice with $\theta = 30°$ and $\psi = 30°$. The third row shows the contour for the hybrid curved hexagonal lattice with $\theta = 30°$ and $\psi = 30°$, $\phi = 45°$, and $L_r = L/2.2$. The slenderness ratio ($\beta = t/L$) is 1/15 for all the cases. L is the length of the corresponding straight constituent beams.

show that this class of lattice can be utilized for low-frequency vibration suppression depending on the design requirements.

Introducing curved and additional elements together drastically influences the wave propagation characteristics of two-dimensional lattices. Following the successful demonstration of this work, future research can exploit various types of additional beams, for example, beams with tip mass, prestressed beams, and functionally graded beams along with curved geometry, for controlling the stop bands in future investigations. Experimental investigations on these lattice metamaterials will be of interest.

CRediT authorship contribution statement

Shuvajit Mukherjee: Conceptualization, Methodology, Writing – original draft, Writing – review & editing, Visualization, Validation, Software, Project administration, Investigation, Formal analysis, Data curation. **Marcus Maeder:** Writing – review & editing. **Milan Cajić:** Writing – review & editing. **Felix Kronowetter:** Writing – review & editing. **Sondipon Adhikari:** Writing – review & editing. **Steffen Marburg:** Writing – review & editing, Resources.

Declaration of competing interest

The authors declare that they have no known competing financial interests or personal relationships that could have appeared to influence the work reported in this paper.

Data availability

No data was used for the research described in the article.

Appendix A. Direct and reciprocal lattice vectors

See Table A.2.
See Fig. A.1.

Appendix B. Bloch's theorem

Let $\mathbf{r}_p$ is a lattice point in the reference unit cell and $\mathbf{w}(\mathbf{r}_p)$ be the displacement of that point corresponding to a plane wave propagating at frequency ω. Then the expression for $\mathbf{w}(\mathbf{r}_p)$ is as follows:

$$\mathbf{w}(\mathbf{r}_p) = \mathbf{w}_{p_0} \mathrm{e}^{\mathrm{i}\omega t - \mathbf{k}\cdot\mathbf{r}_p}, \tag{B.1}$$

where $\mathbf{w}_{p_0}$ and $\mathbf{k}$ denote the wave amplitude and wave vector, respectively. Any other cell can be obtained with respect to the reference unit cell by performing integer translation along the direct lattice vector. For example, the integer pair (n, m) denotes a cell that can be found by translating the n number in the e_1 direction and m in the e_2 direction. The same point p in the (n, m)th cell can be represented as $\boldsymbol{\rho}_p = \mathbf{r}_p + n\mathbf{e}_1 + m\mathbf{e}_2$ ρ. Now, considering Bloch Theorem the displacement of the p th point at (n, m) cell can be written as

$$\mathbf{w}(\boldsymbol{\rho}_p) = \mathbf{w}(\mathbf{r}_p)\mathrm{e}^{\mathbf{k}\cdot(\rho_p - \mathbf{r}_p)} = \mathbf{w}(\mathbf{r}_p)\mathrm{e}^{\mathbf{k}\cdot(n\mathbf{e}_1 + m\mathbf{e}_2)} = \mathbf{w}(\mathbf{r}_p)\mathrm{e}^{nk_1 + mk_2}, \tag{B.2}$$

where $k_i = \mathbf{k}\cdot\mathbf{e}_i$ are the components of the wave vector along the direction of the direct lattice vectors $\mathbf{e}_i$ $(i = 1, 2)$.

Appendix C. The shape function and matrix coefficients

The shape functions for the Timoshenko beam element are adopted from [57]:

$$N_1^u(x) = 1 - \xi, \quad N_2^u(x) = 0, \quad N_3^u(x) = 0, \tag{C.1}$$

$$N_4^u(x) = \xi, \quad N_5^u(x) = 0, \quad N_6^u(x) = 0,$$

Table A.2
Direct ($\mathbf{e}_i$) and reciprocal lattice vectors ($\mathbf{e}_j^*$) of a hexagonal lattice with cell angle θ and the present case with $\theta = 30°$, i, and j are the Cartesian basis for x–y plane. L denotes the length of the straight constituent beam. The direct and reciprocal lattice vectors follow $\mathbf{e}_i \cdot \mathbf{e}_j^* = 2\pi\delta_{ij}$.

Topology	Direct lattice vectors	Reciprocal lattice vectors
Hexagonal lattice	$\mathbf{e}_1 = (L\cos\theta)i + L(1+\sin\theta)j$	$\mathbf{e}_1^* = \frac{2\pi}{2L\cos\theta} i + \frac{2\pi}{2L(1+\sin\theta)} j$
general	$\mathbf{e}_2 = (-L\cos\theta)i + L(1+\sin\theta)j$	$\mathbf{e}_2^* = -\frac{2\pi}{2L\cos\theta} i + \frac{2\pi}{2L(1+\sin\theta)} j$
Hexagonal lattice	$\mathbf{e}_1 = \sqrt{3}L(\frac{1}{2}i + \frac{\sqrt{3}}{2}j)$	$\mathbf{e}_1^* = \frac{2\pi}{\sqrt{3}L}(i + \frac{1}{\sqrt{3}}j)$
$\theta = 30°$	$\mathbf{e}_2 = \sqrt{3}L(-\frac{1}{2}i + \frac{\sqrt{3}}{2}j)$	$\mathbf{e}_2^* = \frac{2\pi}{\sqrt{3}L}(-i + \frac{1}{\sqrt{3}}j)$

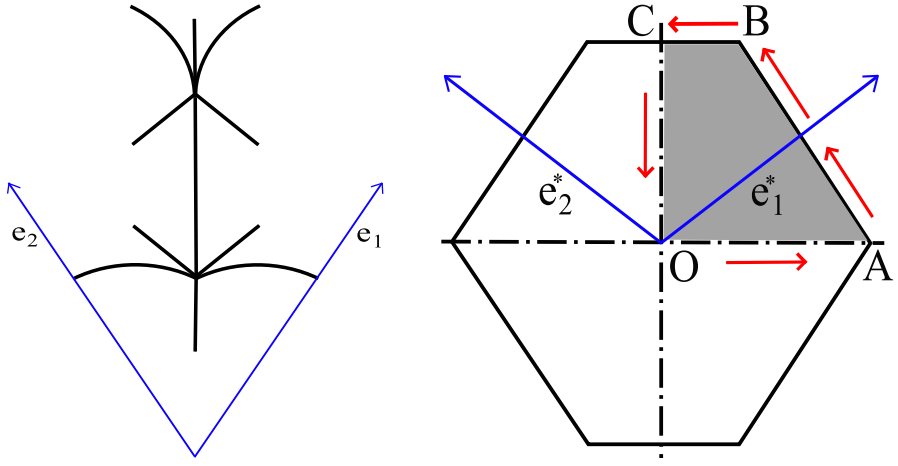

(a) Unit cell of the direct lattice (b) Brillouin zone/unit cell of the reciprocal lattice

Fig. A.1. Figure showing the (a) unit cell with direct lattice vectors ($\mathbf{e}_1$ and $\mathbf{e}_2$) and (b) Brillouin zone, reciprocal lattice vectors ($\mathbf{e}_1^*$ and $\mathbf{e}_2^*$), irreducible Brillouin zone: IBZ (gray part), and its boundary (OABCO).

$$N_1^w(x) = 0, \quad N_2^w(x) = \frac{1 - 3\xi^2 + 2\xi^3 + (1-\xi)\boldsymbol{\Phi}}{1+\boldsymbol{\Phi}},$$
$$N_3^w(x) = \frac{h_e(\xi - 2\xi^2 + \xi^3 + \frac{1}{2}(\xi - \xi^2)\boldsymbol{\Phi})}{1+\boldsymbol{\Phi}}, \tag{C.2}$$

$$N_4^w(x) = 0, \quad N_5^w(x) = \frac{3\xi^2 - 2\xi^3 + \xi\boldsymbol{\Phi}}{1+\boldsymbol{\Phi}}, \quad N_6^w(x) = \frac{h_e(-\xi^2 + \xi^3 - \frac{1}{2}(\xi - \xi^2)\boldsymbol{\Phi})}{1+\boldsymbol{\Phi}},$$

$$N_1^\varphi(x) = 0, \quad N_2^\varphi(x) = \frac{6(-\xi + \xi^2)}{h_e(1+\boldsymbol{\Phi})}, \quad N_3^\varphi(x) = \frac{1 - 4\xi + 3\xi^2 + (1-\xi)\boldsymbol{\Phi}}{1+\boldsymbol{\Phi}}, \tag{C.3}$$

$$N_4^\varphi(x) = 0, \quad N_5^\varphi(x) = \frac{6(\xi - \xi^2)}{h_e(1+\boldsymbol{\Phi})}, \quad N_6^\varphi(x) = \frac{-2\xi + 3\xi^2 + \xi\boldsymbol{\Phi}}{1+\boldsymbol{\Phi}},$$

where $\xi = x/h_e$ denotes the dimensionless axial coordinate and $\boldsymbol{\Phi} = \frac{12EI}{GAk_s h_e^2}$ is the shear deformation parameter.

After adopting these functions, the elements of the stiffness and mass matrix of FE beam model can be written as:

$$K_{ij}^e = \int_0^{h_e} \left[EA \frac{\partial N_i^u}{\partial x}\frac{\partial N_j^u}{\partial x} + EI \frac{\partial N_i^\varphi}{\partial x}\frac{\partial N_j^\varphi}{\partial x} + GAk_s \left(N_i^\varphi - \frac{\partial N_i^w}{\partial x}\right)\left(N_j^\varphi - \frac{\partial N_j^w}{\partial x}\right)\right] \mathrm{d}x, \tag{C.4}$$

$$M_{ij}^e = \int_0^{h_e} \left(\rho A N_i^u N_j^u + \rho I N_i^\varphi N_j^\varphi + \rho A N_i^w N_j^w\right) \mathrm{d}x. \tag{C.5}$$

References

[1] Lee J-H, Singer JP, Thomas EL. Micro-/nanostructured mechanical metamaterials. Adv Mater 2012;24(36):4782–810.

[2] Zheng X, Lee H, Weisgraber TH, Shusteff M, DeOtte J, Duoss EB, et al. Ultralight, ultrastiff mechanical metamaterials. Science 2014;344(6190):1373–7.

[3] Helou M, Kara S. Design, analysis and manufacturing of lattice structures: an overview. Int J Comput Integr Manuf 2018;31(3):243–61.

[4] Jiang W, Yin G, Xie L, Yin M. Multifunctional 3D lattice metamaterials for vibration mitigation and energy absorption. Int J Mech Sci 2022;233:107678.

[5] Kronowetter F, Wagner P, Kolodi J, Brabandt I, Neumeyer T, Rümmler N, et al. Novel compound material and metamaterial wheelhouse liners for tire noise reduction. Mech Syst Signal Process 2023;200:110548.

[6] Gibson LJ. Cellular solids. Bulletin 2003;28(4):270–4.

[7] Ai L, Gao X-L. Metamaterials with negative Poisson's ratio and non-positive thermal expansion. Compos Struct 2017;162:70–84.

[8] An X, Lai C, Fan H, Zhang C. 3D acoustic metamaterial-based mechanical metalattice structures for low-frequency and broadband vibration attenuation. Int J Solids Struct 2020;191:293–306.

[9] Chen X, Ji Q, Wei J, Tan H, Yu J, Zhang P, et al. Light-weight shell-lattice metamaterials for mechanical shock absorption. Int J Mech Sci 2020;169:105288.

[10] Kronowetter F, Maeder M, Chiang YK, Huang L, Schmid JD, Oberst S, et al. Realistic prediction and engineering of high-Q modes to implement stable Fano resonances in acoustic devices. Nature Commun 2023;14(1):6847.

[11] Teng XC, Ren X, Zhang Y, Jiang W, Pan Y, Zhang XG, et al. A simple 3D re-entrant auxetic metamaterial with enhanced energy absorption. Int J Mech Sci 2022;229:107524.

[12] Alomar Z, Concli F. A review of the selective laser melting lattice structures and their numerical models. Adv Energy Mater 2020;22(12):2000611.

[13] Sigalas MM. Elastic and acoustic wave band structure. J Sound Vib 1992;158(2):377–82.

[14] Phani AS, Woodhouse J, Fleck N. Wave propagation in two-dimensional periodic lattices. J Acoust Soc Am 2006;119(4):1995–2005.

[15] Zhang K, Zhao P, Zhao C, Hong F, Deng Z. Study on the mechanism of band gap and directional wave propagation of the auxetic chiral lattices. Compos Struct 2020;238:111952.

[16] Iwata Y, Yokozeki T. Wave propagation analysis of one-dimensional CFRP lattice structure. Compos Struct 2021;261:113306.

[17] An X, Fan H, Zhang C. Elastic wave and vibration bandgaps in planar square metamaterial-based lattice structures. J Sound Vib 2020;475:115292.

[18] Ruzzene M, Scarpa F, Soranna F. Wave beaming effects in two-dimensional cellular structures. Smart Mater Struct 2003;12(3):363.

[19] Spadoni A, Ruzzene M, Gonella S, Scarpa F. Phononic properties of hexagonal chiral lattices. Wave Motion 2009;46(7):435–50.
[20] Shim J, Wang P, Bertoldi K. Harnessing instability-induced pattern transformation to design tunable phononic crystals. Int J Solids Struct 2015;58:52–61.
[21] Gao C, Slesarenko V, Boyce MC, Rudykh S, Li Y. Instability-induced pattern transformation in soft metamaterial with hexagonal networks for tunable wave propagation. Sci Rep 2018;8(1):11834.
[22] Gonella S, Ruzzene M. Analysis of in-plane wave propagation in hexagonal and re-entrant lattices. J Sound Vib 2008;312(1–2):125–39.
[23] Sigmund O, Søndergaard Jensen J. Systematic design of phononic band–gap materials and structures by topology optimization. Philos Trans R Soc Lond Ser A Math Phys Eng Sci 2003;361(1806):1001–19.
[24] Swartz KE, White DA, Tortorelli DA, James KA. Topology optimization of 3D photonic crystals with complete bandgaps. Opt Express 2021;29(14):22170–91.
[25] Gao H, Qu Y, Meng G. Topology optimization and wave propagation of three-dimensional phononic crystals. J Vib Acoust 2022;1–31.
[26] Mukherjee S, Scarpa F, Gopalakrishnan S. Phononic band gap design in honeycomb lattice with combinations of auxetic and conventional core. Smart Mater Struct 2016;25(5):054011.
[27] Yan G, Yao S, Li Y. Propagation of elastic waves in metamaterial plates with various lattices for low-frequency vibration attenuation. J Sound Vib 2022;536:117140.
[28] Baravelli E, Ruzzene M. Internally resonating lattices for bandgap generation and low-frequency vibration control. J Sound Vib 2013;332(25):6562–79.
[29] Li Y, Zhao N, Yao S. Theoretical analysis of 2D meta-structure with inertia amplification. Int J Mech Sci 2022;235:107717.
[30] Zhang K, Zhao P, Hong F, Yu Y, Deng Z. On the directional wave propagation in the tetrachiral and hexachiral lattices with local resonators. Smart Mater Struct 2019;29(1):015017.
[31] Meng J, Deng Z, Zhang K, Xu X. Wave propagation in hexagonal and re-entrant lattice structures with cell walls of non-uniform thickness. Waves Random Complex Media 2015;25(2):223–42.
[32] Bortot E, Amir O, Shmuel G. Topology optimization of dielectric elastomers for wide tunable band gaps. Int J Solids Struct 2018;143:262–73.
[33] Bacigalupo A, Lepidi M, Gnecco G, Vadalà F, Gambarotta L. Optimal design of the band structure for beam lattice metamaterials. Front Mater 2019;6:2.
[34] Dalklint A, Wallin M, Bertoldi K, Tortorelli D. Tunable phononic bandgap materials designed via topology optimization. J Mech Phys Solids 2022;163:104849.
[35] Cheng Q, Guo H, Yuan T, Sun P, Guo F, Wang Y. Topological design of square lattice structure for broad and multiple band gaps in low-frequency range. Extreme Mech Lett 2020;35:100632.
[36] Yan G, Yao S, Li Y, Zhou W. Topological optimization of thin elastic metamaterial plates for ultrawide flexural vibration bandgaps. Int J Mech Sci 2023;242:108014.
[37] Lim QJ, Wang P, Koh SJA, Khoo EH, Bertoldi K. Wave propagation in fractal-inspired self-similar beam lattices. Appl Phys Lett 2015;107(22):221911.
[38] Zhao P, Zhang K, Zhao C, Deng Z. Mechanism of band gaps in self-similar triangular lattice with koch fractal. J Vib Acoust 2022;144(3).
[39] Miniaci M, Krushynska A, Movchan AB, Bosia F, Pugno NM. Spider web-inspired acoustic metamaterials. Appl Phys Lett 2016;109(7):071905.
[40] Trainiti G, Rimoli JJ, Ruzzene M. Wave propagation in undulated structural lattices. Int J Solids Struct 2016;97:431–44.
[41] Wang Y-F, Wang Y-S, Zhang C. Bandgaps and directional properties of two-dimensional square beam-like zigzag lattices. AIP Adv 2014;4(12):124403.
[42] Wang Y-F, Wang Y-S, Zhang C. Bandgaps and directional propagation of elastic waves in 2D square zigzag lattice structures. J Phys D: Appl Phys 2014;47(48):485102.
[43] Mukherjee S, Adhikari S. The in-plane mechanics of a family of curved 2D lattices. Compos Struct 2022;280:114859.
[44] Zhang K, Zhao C, Zhao P, Luo J, Deng Z. Wave propagation properties of rotationally symmetric lattices with curved beams. J Acoust Soc Am 2020;148(3):1567–84.
[45] Fu Y, Liu W. Design of mechanical metamaterial with controllable stiffness using curved beam unit cells. Compos Struct 2021;258:113195.
[46] Zhu Z, Deng Z, Huang B, Du J. Elastic wave propagation in triangular chiral lattices: Geometric frustration behavior of standing wave modes. Int J Solids Struct 2019;158:40–51.
[47] Qi D, Yu H, Hu W, He C, Wu W, Ma Y. Bandgap and wave attenuation mechanisms of innovative reentrant and anti-chiral hybrid auxetic metastructure. Extreme Mech Lett 2019;28:58–68.
[48] Prasad R, Baxy A, Banerjee A. Two-dimensional in-plane elastic waves in curved-tapered square lattice frame structure. J Appl Mech 2022;89(3).
[49] Li Y, Yan G. Vibration characteristics of innovative reentrant-chiral elastic metamaterials. Eur J Mech A Solids 2021;90:104350.
[50] Ruan H, Hou J, Li D. Wave propagation characterization of 2D composite chiral lattice structures with circular plate inclusions. Eng Struct 2022;264:114466.
[51] Guo L, Liu J, Gao N, Huang Q, Pan G, Song B. Wave propagation behaviors of a low-symmetry reentrant chiral structure with mass inclusion in a single material. Eur J Mech A Solids 2023;99:104951.
[52] Mukherjee S, Cajić M, Karličić D, Adhikari S. Enhancement of band-gap characteristics in hexagonal and re-entrant lattices via curved beams. Compos Struct 2023;306:116591.
[53] Slesarenko V. Bandgap structure in elastic metamaterials with curvy Bezier beams. Appl Phys Lett 2023;123(8).
[54] Karličić D, Cajić M, Chatterjee T, Adhikari S. Wave propagation in mass embedded and pre-stressed hexagonal lattices. Compos Struct 2021;256:113087.
[55] Liu W, Chen J-W, Su X-Y. Local resonance phononic band gaps in modified two-dimensional lattice materials. Acta Mech Sin 2012;28(3):659–69.
[56] Cazzani A, Stochino F, Turco E. On the whole spectrum of timoshenko beams. Part I: a theoretical revisitation. Z Angew Math Phys 2016;67:1–30.
[57] Yokoyama T. Vibration analysis of timoshenko beam-columns on two-parameter elastic foundations. Comput Struct 1996;61(6):995–1007.
[58] Kittel C, McEuen P. Kittel's Introduction to Solid State Physics. John Wiley & Sons; 2018.
[59] Zelhofer AJ, Kochmann DM. On acoustic wave beaming in two-dimensional structural lattices. Int J Solids Struct 2017;115:248–69.